Generalized Multivariable Grid-Forming Control Design for Power Converters

Meng Chen, *Member, IEEE*, Dao Zhou, *Senior Member, IEEE*, Ali Tayyebi, Eduardo Prieto-Araujo, *Senior Member, IEEE*, Florian Dörfler, *Senior Member, IEEE*, and Frede Blaabjerg, *Fellow, IEEE*

***Abstract*—The grid-forming converter is an important unit in the future power system with more inverter-interfaced generators. However, improving its performance is still a key challenge. This paper proposes a generalized architecture of the grid-forming converter from the view of multivariable feedback control. As a result, many of the existing popular control strategies, i.e., droop control, power synchronization control, virtual synchronous generator control, matching control, dispatchable virtual oscillator control, and their improved forms are unified into a multivariable feedback control transfer matrix working on several linear and nonlinear error signals. Meanwhile, unlike the traditional assumptions of decoupling between AC and DC control, active power and reactive power control, the proposed configuration simultaneously takes all of them into consideration, which therefore can provide better performance. As an example, a new multi-input-multi-output-based grid-forming (MIMO-GFM) control is proposed based on the generalized configuration. To cope with the multivariable feedback, an optimal and structured $\mathcal{H}_\infty$ synthesis is used to design the control parameters. At last, simulation and experimental results show superior performance and robustness of the proposed configuration and control.**

***Index Terms*—Grid-forming, power converter, multiple-input-multiple-output system, feedback control, $\mathcal{H}_\infty$ synthesis.**

I. Introduction

THE CONVENTIONAL power system is evolving into a future smart grid, which relies on the advanced technologies in power systems, power electronics, information and communication technology, etc. One of the most important tasks of the smart grid is to enable a robust integration of various renewable energies and energy storage systems. As most of these are interfaced via power inverters, the control of power inverters plays a fundamental role to ensure the requirements of the smart grid on stable, flexible, and efficient power regulation [1]–[3].

As more inverter-interfaced generators (IIGs) are integrated into the smart grid, stability issues are becoming more pronounced due to the lack of inertia and poor regulation of the frequency and voltage. To cope with these challenges, grid-forming converters can establish the frequency and voltage by themselves without relying on the power grid. The synchronization among the grid-forming converters and with the power grid is based on the power balance rather than on a phase-locked loop (PLL) like in a traditional grid-following converter. Therefore, by proper power control, grid-forming converters are able to participate in the frequency and voltage regulation and then help to enlarge the penetration of the IIGs in the power system. On the contrary, the stability of the power system may be deteriorated if the control of the grid-forming converter is not well designed [4].

So far, several grid-forming controls have been proposed, where a classification is summarized as follows. The basic one is droop control, which emulate the *p-f* and *q-V* droop characteristics of the synchronous generator (SG) to achieve frequency and voltage regulation [5]. A similar idea is called power synchronization control (PSC), which directly builds the relationship between the active power and the angle like the synchronous generator as well [6]. To improve the dynamic performance by limiting the fast change of the frequency, the virtual synchronous generator (VSG) control has been proposed, which not only has the droop characteristics but also can provide the favorable inertia characteristics [7] for small rate of change of frequency (RoCoF). Another interesting grid-forming control is matching control. The motivation is that the dynamics of the DC capacitor are similar to the swing equation of the synchronous generator, and the frequency can be built by the DC voltage [8]. In contrast with the aforementioned SG-emulation methods, a dispatchable virtual oscillator control (dVOC) is also proposed to treat the grid-forming converters as coupled oscillators [9]. More recently, a hybrid angle control (HAC) is proposed in [10], which uses nonlinear controllers and combines the DC and AC dynamics to give superior performance.

Manuscript received September 8, 2021; revised January 26, 2022; accepted March 19, 2022. Date of publication March 22, 2022; date of current version June 21, 2022. This work was supported in part by the Reliable Power Electronic-Based Power System (REPEPS) Project at AAU Energy, Aalborg University as part of the Villum Investigator Program funded by the Villum Foundation and in part by the Austrian Institute for Technology, HER, and ETH Zürich. Paper no. TSG-01445-2021. *(Corresponding author: Meng Chen.)*

Meng Chen, Dao Zhou, and Frede Blaabjerg are with the AAU Energy, Aalborg University, 9220 Aalborg, Denmark (e-mail: mche@energy.aau.dk; zda@energy.aau.dk; fbl@energy.aau.dk).

Ali Tayyebi is with Hitachi Energy Research, 72226 Västerås, Sweden, and also with the Automatic Control Laboratory, ETH Zürich, 8092 Zürich, Switzerland (e-mail: ali.tayyebi@hitachienergy.com).

Eduardo Prieto-Araujo is with the CITCEA-UPC and the Serra Húnter Programme, Technical University of Catalonia, 08028 Barcelona, Spain (e-mail: eduardo.prieto-araujo@upc.edu).

Florian Dörfler is with the Automatic Control Laboratory, ETH Zürich, 8092 Zürich, Switzerland (e-mail: dorfler@ethz.ch).

Color versions of one or more figures in this article are available at https://doi.org/10.1109/TSG.2022.3161608.

Digital Object Identifier 10.1109/TSG.2022.3161608

Based on the aforementioned fundamental controls, many improved methods have been reported in the literature in order to provide better performance. A robust droop control is proposed in [11], where an additional voltage feedback is added to improve the accuracy of power sharing. Further in [12], a more additional frequency feedback is added as well. A generalized droop control is proposed by replacing the fixed gain with transfer functions in [13] to improve the performance of the closed-loop system. By changing the integral (I) controller to the proportional-integral (PI) controller, the virtual inertia is included in the PSC in [14]. In [15], a generalized PSC is designed, which can also integrate both the droop and inertia characteristics. In [16], a novel PSC is proposed in order to freely adjust the damping. In [17] and [18], the high-frequency component of the frequency is used to improve the damping of the VSG. In [19] and [20], the coupling terms of the voltage and frequency are designed to enhance the stability of the VSG, respectively. In [21], the DC voltage is also used to provide additional damping for the matching control. Other improved grid-forming controllers have been presented in [22]–[26]. Given the numerous grid-forming controllers and their variations, it is hard to compare and evaluate these methods. Therefore, it is important to study the relationships among different grid-forming methods as well as to unify and generalize their control architectures.

In [27], generalized grid-connected controls encompassing droop control have been proposed. The initial and most tries for unifying grid-forming controls are focusing on the basic droop control with low-pass filters (LPFs) and the VSG control. It has been proven that they are identical in some cases for properly selected parameters [7], [28]. In [13], the droop control and the VSG are unified by analyzing different damping terms. The basic droop control and the PSC control are also shown to be identical to some extent [6]. Besides, a unified modeling method is presented in [24] focusing on several VSG controls from the view of frequency control. On the contrary, different voltage controls of the VSG are compared in [25]. By considering more kinds of grid-forming controllers, a comprehensive comparison is given in [9], while no commonalities are highlighted. In [29], the different grid-forming controllers are summarized from a block diagram perspective by a power synchronization loop and a voltage profile management. Nevertheless, the common structures of these two parts are not further discussed. More important, the structure of [29] assumes that the *p-f* loop and *Q-V* loop are decoupled. Likewise, the DC loop is not included.

According to the above discussion, the existing works on unifying the grid-forming controllers have limitations in four aspects. First, most of the studies consider only the basic control architectures, while their improved variations cannot be included. Second, only one or two kinds but not all of the grid-forming controllers have been unified within in a single architecture so far including DC and AC side loops. Third, only single-input-single-output (SISO) loops are considered, i.e., most of the studies assume that the DC and AC sides and the active and reactive power loops are decoupled, which is not true in reality. Fourth, manual parameter tuning of many nested single-input-single-output (SISO) loops is usually burdensome and cannot achieve the optimal control performance for a multi-input-multi-output (MIMO) system [30].

In order to overcome the aforementioned limitations, this paper looks at the grid-forming converter design from the perspective of modern control theory. First, the grid-forming converter is abstracted as a general MIMO system. Then a multivariable feedback control architecture is proposed to provide a generalized configuration, which results in the following advantages.

1) The proposed configuration unifies and generalizes different grid-forming controls - not only the basic formulations, but also many of their improved variations - in a control transfer matrix relating on several linear and nonlinear error signals.
2) The comparisons between different grid-forming controls can be performed in a straightforward way.
3) Different loops, e.g., DC control, active power control, and reactive power control of the grid-forming controls can be tuned simultaneously to optimize the performance and robustness.
4) New grid-forming controls can be derived from the proposed generalized configuration.

To further highlight the design power of the proposed generalized configuration, a new multi-input-multi-output-based grid-forming (MIMO-GFM) control is also proposed in this paper, which improves the performance without increasing the order of the controllers compared with the existing basic control such as VSG and droop with LPF. Usually, classic control design methods such as root locus and loop shaping are used to design the parameters. However, they cannot deal with several adjustable parameters simultaneously to obtain the optimal performance especially in a MIMO system. As a solution, the $\mathcal{H}_\infty$ synthesis can be used, which has been proved to be effective in secondary frequency control [31], current control of grid-following converter [32], and voltage control of PLL or droop based grid-connected converters [27], etc. Nevertheless, no use in the MIMO-GFM converter including all the three control loops has been reported. In this paper, we present how the proposed MIMO-GFM controller can be transformed to the standard $\mathcal{H}_\infty$ synthesis, where the fixed-structure $\mathcal{H}_\infty$ synthesis is performed to optimize the parameters of the controller.

The remainder of the paper is organized as follows: Section II presents the proposed generalized configuration and unifies the existing grid-forming controllers. Section III proposes a new MIMO-GFM controller and gives the details of parameters design based on the $\mathcal{H}_\infty$ synthesis. Simulations and experimental results are performed in Section IV, and the conclusions are drawn in Section V.

II. General Configuration of Grid-Forming Converter

The studied topology of the grid-forming converter is a typical three-phase voltage-source inverter as shown in Fig. 1. This topology has many applications, where most of the existing research on the grid-forming converter are based on it [5], [6], [8], [12]. Therefore, it is a representative topology.

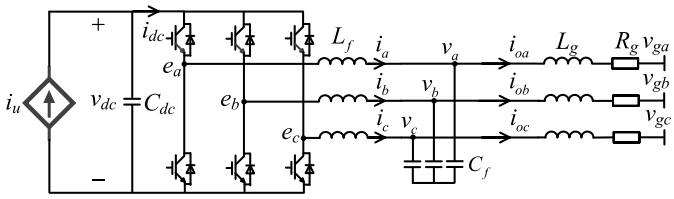

Fig. 1. Topology of grid-forming converter.

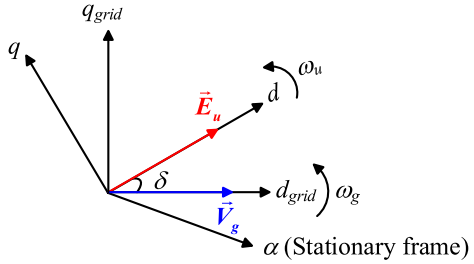

Fig. 2. Relationships of different reference frames.

The three-phase inverter is connected to the power grid via a filter. L_f and C_f are the inductor and capacitor of the filter. L_g and R_g are the equivalent inductor and resistor to the power grid. Most of the existing works assume that the DC source is ideal and able to decouple the AC and DC sides. Although this assumption simplifies the analysis, the information in the dynamics of the DC capacitor is missing, which can be used to improve the performance. Meanwhile, some grid-forming controls such as the matching control is based on the coupling between AC and DC sides. Therefore, in this paper, the dynamics of the capacitor are included, where the DC source is equivalent to a controlled current source i_u paralleled with a capacitor C_{dc} [9].

A. MIMO Formulation of Grid-Forming Converter

The modeling of AC side of the grid-forming converter can be built in different frames, which can be illustrated in Fig. 2. If the d_{grid}-q_{grid} frame is used as the reference frame, there are $[V_{gd}; V_{gq}] = [V_g; 0]$ and $[E_{gd}; E_{gq}] = [E_u cos\delta; E_u sin\delta]$. If the d-q frame is used, there are $[V_{gd}; V_{gq}] = [V_g cos\delta; -V_g sin\delta]$ and $[E_{gd}; E_{gq}] = [E_u; 0]$. They are identical by proper transformations [17]. This paper chooses the second set of coordinates and the model is summarized as follows [12], [13], [17]:

$$\dot{i}_d = \frac{\omega_b}{L_f}E_u - \frac{\omega_b}{L_f}v_d + \omega_b\omega_u i_q \tag{1}$$

$$\dot{i}_q = -\frac{\omega_b}{L_f}v_q - \omega_b\omega_u i_d \tag{2}$$

$$\dot{v}_d = \frac{\omega_b}{C_f}i_d - \frac{\omega_b}{C_f}i_{od} + \omega_b\omega_u v_q \tag{3}$$

$$\dot{v}_q = \frac{\omega_b}{C_f}i_q - \frac{\omega_b}{C_f}i_{oq} - \omega_b\omega_u v_d \tag{4}$$

$$\dot{i}_{od} = \frac{\omega_b}{L_g}v_d - \frac{\omega_b}{L_g}V_g\cos\delta - \frac{\omega_b R_g}{L_g}i_{od} + \omega_b\omega_u i_{oq} \tag{5}$$

$$\dot{i}_{oq} = \frac{\omega_b}{L_g}v_q + \frac{\omega_b}{L_g}V_g\sin\delta - \frac{\omega_b R_g}{L_g}i_{oq} - \omega_b\omega_u i_{od} \tag{6}$$

where i_{dq}, v_{dq}, and i_{odq} are the currents of the filter inductor, voltages of the filter capacitor, and output currents, respectively, ω_b is the base angular frequency, V_g is the voltage

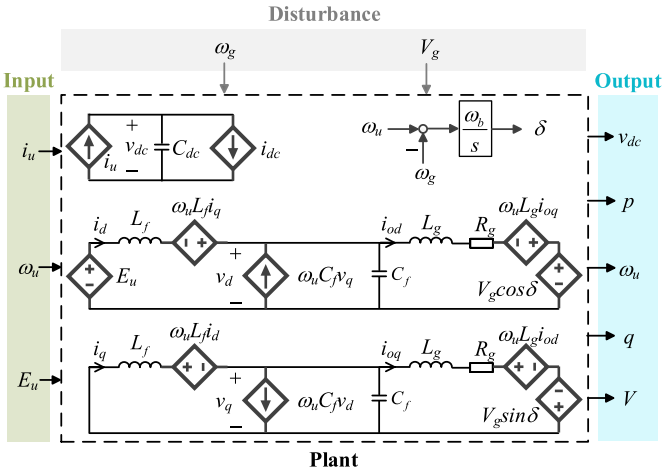

Fig. 3. MIMO open-loop equivalent circuit of grid-forming converter in d-q frame.

magnitude of the power grid, ω_u and E_u are the frequency and voltage provided by the grid-forming control, δ is the angle difference between the grid-forming converter and the power grid, which is defined as

$$\dot{\delta} = \omega_b\omega_u - \omega_b\omega_g, \tag{7}$$

where ω_g is the angular frequency of the power grid. Furthermore, the DC dynamics are modeled as

$$\dot{v}_{dc} = \frac{\omega_b}{C_{dc}}i_u - \frac{\omega_b E_u i_d}{C_{dc}v_{dc}}, \tag{8}$$

where v_{dc} is the DC voltage. It is noted that the DC dynamics contain the information of the AC side by $E_u i_d$, which provides the possibility to improve the AC performance by the DC signals. We stress that, the usual assumption of ideal DC source is not beneficial to optimize the grid-forming converter.

For the grid-forming converter, five outputs are usually considered, i.e., the active and reactive power p and q, magnitude of the terminal voltage V, the frequency assigned by the grid-forming control ω_u, as well as v_{dc}, where p, q, V are expressed by the state variables as follows:

$$p = v_d i_{od} + v_q i_{oq} \tag{9}$$

$$q = -v_d i_{oq} + v_q i_{od} \tag{10}$$

$$V = \sqrt{v_d^2 + v_q^2}. \tag{11}$$

Hence, the open-loop equivalent circuit of the grid-forming converter can be represented by a MIMO system, as shown in Fig. 3. There are three control inputs, which should be provided by the grid-forming control, and five outputs, which should be regulated. Furthermore, the grid voltage and frequency can be seen as disturbances. It should be mentioned that all the variables and parameters in (1)–(11) are presented in the p.u. system except that ω_b and δ are with the physical units of rad/s and rad, respectively. The nominal values of the power converter are chosen as the base quantities of the p.u. system.

For notational convenience, we define the vectors:

$$\boldsymbol{x} = \begin{bmatrix} i_d & i_q & v_d & v_q & i_{od} & i_{oq} & \delta & v_{dc} \end{bmatrix}^T \tag{12}$$

$$\boldsymbol{u} = \begin{bmatrix} i_u & \omega_u & E_u \end{bmatrix}^T \tag{13}$$

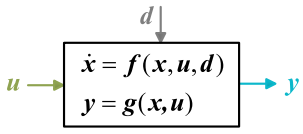

Fig. 4. MIMO open-loop state-space model of grid-forming converter.

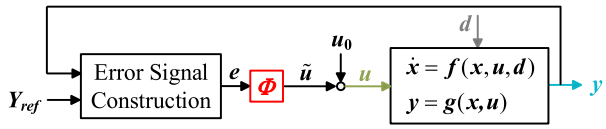

Fig. 5. General MIMO close-loop feedback control configuration of grid-forming converter.

$$\boldsymbol{y} = \begin{bmatrix} v_{dc} & p & \omega_u & q & V \end{bmatrix}^T \tag{14}$$

$$\boldsymbol{d} = \begin{bmatrix} \omega_g & V_g \end{bmatrix}^T, \tag{15}$$

where $\boldsymbol{x}$ is the state vector, $\boldsymbol{u}$ is the control vector, $\boldsymbol{y}$ is the output vector, and $\boldsymbol{d}$ is the disturbance vector. Thereafter, the equivalent circuit of Fig. 3 can be abstracted as the open-loop state-space model as shown in Fig. 4, from which the target of the grid-forming control is defined as the following.

A grid-forming control is to design a control input **u** for the system (**f**, **g**) to guarantee that the output **y** satisfies the desired specifications (details will be given later in Section III) in the presence of disturbance **d**.

To cope with this problem, a multivariable feedback control can be used to close the loop. Therefore, a generalized configuration of the grid-forming converter control architecture is proposed, as shown in Fig. 5,

$$\boldsymbol{u_0} = \begin{bmatrix} i_0 & \omega_0 & E_0 \end{bmatrix}^T \tag{16}$$

$$\boldsymbol{Y}_{ref} = \begin{bmatrix} V_{dcref} & P_{ref} & \omega_g & Q_{ref} & V_{ref} \end{bmatrix}^T \tag{17}$$

$$\boldsymbol{\Phi} = \left(\phi_{ij}\right)_{3\times 5}, \tag{18}$$

where $\boldsymbol{u_0}$ is the vector of set-points for $\boldsymbol{u}$, $\boldsymbol{Y}_{ref}$ is the vector of references for $\boldsymbol{y}$. We notice that the nominal reference of the frequency is chosen as ω_g due to the fact that the frequency of the grid-forming converter should be synchronized to the grid frequency in the nominal steady-state. Besides, $\boldsymbol{\Phi} = \boldsymbol{\Phi}(s)$ is the 3×5 control transfer matrix, and $\boldsymbol{e}$ is the vector of error signals. The achievement of the grid-forming controller is therefore attributed to the choices of $\boldsymbol{\Phi}$ and $\boldsymbol{e}$. A simple and natural choice of $\boldsymbol{e}$ is using the linear error signals, i.e., $\boldsymbol{e} = \boldsymbol{Y}_{ref} - \boldsymbol{y}$. Nevertheless, some nonlinear error signals can also prove useful, which will be discussed later.

It should be mentioned that the general configuration in Fig. 5 can be easily used to other converter structure with L filter, LC filter, LCL filter, etc., by replacing the three-phase converter model with the model of the used structure, i.e., changing only $\dot{\boldsymbol{x}} = \boldsymbol{f}(\boldsymbol{x}, \boldsymbol{u}, \boldsymbol{d})$ and $\boldsymbol{y} = \boldsymbol{g}(\boldsymbol{x}, \boldsymbol{u})$. Meanwhile, the model can also be built in α-β frame or *abc* frame as shown in Fig. 6. However, the above changes do not influence the discussion on the control transfer matrix $\boldsymbol{\Phi}$ [11], [29], which is the main contribution of this paper.

To highlight the advantages, the following section will discuss how the existing methods are unified by the proposed generalized configuration of the grid-forming converter.

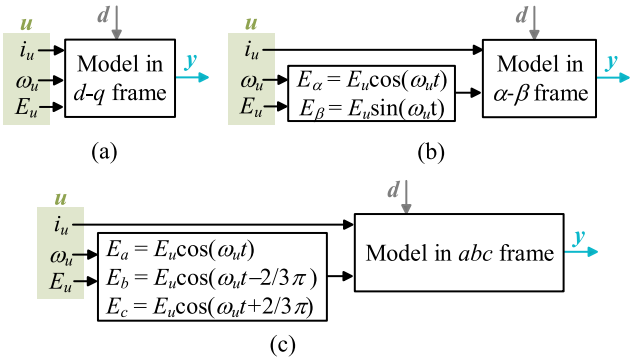

Fig. 6. MIMO open-loop state-space model of grid-forming converter in different frames. (a) d-q frame. (b) α-β frame. (c) *abc* frame.

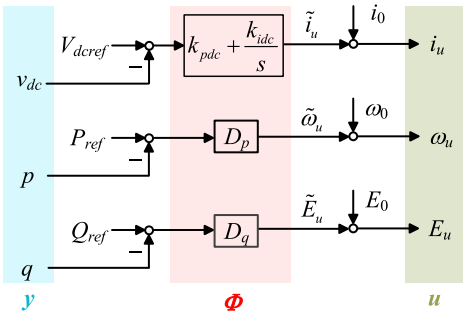

Fig. 7. Block diagram of droop control.

B. Discussion on Existing Grid-Forming Converters

1) Droop Control: Droop control emulates the droop characteristics of the regulation of SG, which can be expressed as [5], [6]

$$\omega_u - \omega_0 = -D_p\left(p - P_{ref}\right) \tag{19}$$

$$E_u - E_0 = -D_q\left(q - Q_{ref}\right), \tag{20}$$

where D_p and D_q are the droop coefficients. As mentioned before, the general strategy the droop control assumes an ideal DC source and therefore neglect the DC control. This paper removes this assumption. In practice, a proportional integral (PI) controller is usually used to control the voltage of the DC capacitor, which is expressed as

$$i_u = i_0 + k_{pdc}\left(V_{dcref} - v_{dc}\right) + k_{idc}\int\left(V_{dcref} - v_{dc}\right)dt, \tag{21}$$

where k_{pdc} and k_{idc} are the proportional and integral gains, respectively.

According to (19)-(21), the equivalent control block of the droop control using the generalized configuration is shown in Fig. 7, where the control transfer matrix is

$$\boldsymbol{\Phi} = \begin{bmatrix} k_{pdc} + k_{idc}/s & 0 & 0 & 0 & 0 \\ 0 & D_p & 0 & 0 & 0 \\ 0 & 0 & 0 & D_q & 0 \end{bmatrix}. \tag{22}$$

The control transfer matrix of droop control (22) uses a SISO PI controller and two SISO proportional (P) controllers to derive the grid-forming control input, and there is no coupling between different columns and rows. Therefore, effective (v_{dc}, p, ω_u, q, V) coupling that exists in reality is typically not considered.

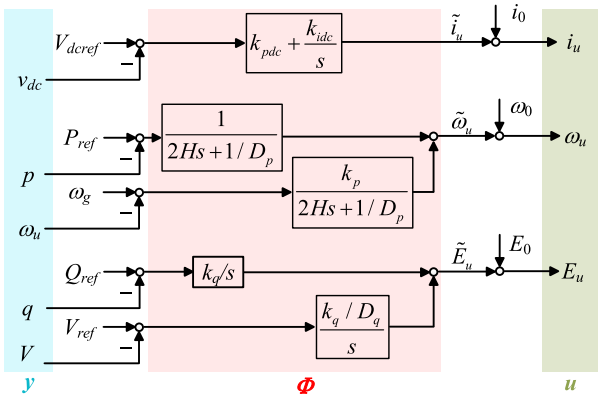

Fig. 8. Block diagram of VSG control.

2) PSC Control: The PSC control directly emulates the relationship between the rotor angle and the active power of the SG, which can be expressed as [6]

$$D_p \int (P_{ref} - p)dt + \omega_0 t = \int \omega_u dt \tag{23}$$

which can be rewritten in the form of the general configuration, by solving for ω_u, as

$$D_p(P_{ref} - p) + \omega_0 = \omega_u \tag{24}$$

By comparing (24) with (19), we conclude that PSC control is equivalent to droop control with respect to ω_u. Moreover, the DC and AC voltage controls of PSC control can also be chosen to be identical as in droop control. Therefore, the control transfer matrix of the PSC control has the same structure as droop control in (22).

3) VSG Control: The VSG control emulate the SG in a more detailed fashion than droop control and PSC control. One of basic architectures can be expressed as [24], [25], [33]

$$2H\Delta\dot{\omega}_u = P_{ref} - p - \frac{1}{D_p}(\omega_u - \omega_0) - k_p(\omega_u - \omega_g) \tag{25}$$

$$k_q \int \left[Q_{ref} - q + \frac{1}{D_q}(V_{ref} - V)\right]dt + E_0 = E_u, \tag{26}$$

where the inertia constant H emulates the inertia characteristics and the damping coefficient k_p emulates the damping characteristics. Furthermore, the DC control is usually based on a PI control, as in (21). Therefore, the equivalent control block of the VSG control using the generalized configuration is shown in Fig. 8, where the control transfer matrix is

$$\mathbf{\Phi} = \begin{bmatrix} k_{pdc} + k_{idc}/s & 0 & 0 & 0 & 0 \\ 0 & \frac{1}{2Hs+1/D_p} & \frac{k_p}{2Hs+1/D_p} & 0 & 0 \\ 0 & 0 & 0 & k_q/s & \frac{k_q/D_q}{s} \end{bmatrix}. \tag{27}$$

The control transfer matrix (27) of the VSG uses PI controller, low-pass filters (LPFs), and I controllers to derive the control inputs, respectively, and there are again no coupling terms among different rows, i.e., the couplings among DC voltage, AC voltage, and frequency controls are not considered.

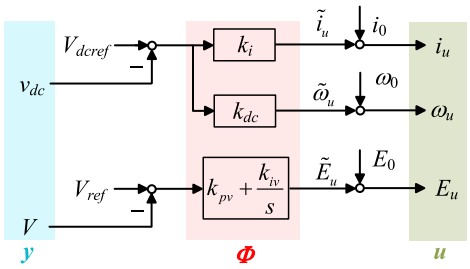

Fig. 9. Block diagram of matching control.

4) Matching Control: The matching control is motivated by the fact that the dynamics of the DC capacitor are similar to the rotor in the SG, and therefore ω_u can be generated by v_{dc}. The mathematical model of the matching control can be expressed as [8]

$$i_u = i_0 + k_i(V_{dcref} - v_{dc}) \tag{28}$$

$$\omega_u = \omega_0 + k_{dc}(V_{dcref} - v_{dc}) \tag{29}$$

$$k_{pv}(V_{ref} - V) + k_{iv} \int (V_{ref} - V)dt + E_0 = E_u \tag{30}$$

based on which the equivalent control block using the generalized configuration is shown in Fig. 9. Thereafter, the control transfer matrix of the matching control can be derived as

$$\mathbf{\Phi} = \begin{bmatrix} k_i & 0 & 0 & 0 & 0 \\ k_{dc} & 0 & 0 & 0 & 0 \\ 0 & 0 & 0 & 0 & k_{pv} + k_{iv}/s \end{bmatrix}. \tag{31}$$

The matrix of the matching control uses two P controllers and one PI controller to derive the control inputs. Note that the first two rows are coupled via the DC signal.

The above analysis shows how a selection of the basic grid-forming controllers can be transformed to the proposed generalized configuration. These original non-matrix-based controllers typically in the form of block diagrams are mathematically equivalent to the corresponding representations of the control transfer matrix. By analogous reasoning also their various improved formulations can be represented as particular control transfer matrices. Table I summarizes the control transfer matrices employed in different grid-forming controllers.

C. Discussion on Proposed Generalized Configuration

According to the aforementioned analysis, the following advantages of the proposed generalized configuration of the grid-forming converter can be concluded.

1) Not only the basic formulations of the grid-forming controls, but also many of their improved variations can be presented as control transfer matrices in a unified setting.
2) The comparisons between different grid-forming controls is straightforward. From Table I, it can be deduced how the performance may improve by changing the elements of the control transfer matrix. A typical strategy is using higher-order controllers, especially in the frequency control of deriving ω_u. Meanwhile, the relationships between different controls are obvious. For

TABLE I
SUMMARY OF CONTROL TRANSFER MATRICES CORRESPONDING TO DIFFERENT GRID-FORMING CONTROLLERS

Feedback Signals $\boldsymbol{y}$	v_{dc}	p	ω_u	q	V	v_{dc}	p	ω_u	q	V	v_{dc}	p	ω_u	q	V
Transfer Matrix ϕ_{ij}	ϕ_{11}	ϕ_{12}	ϕ_{13}	ϕ_{14}	ϕ_{15}	ϕ_{21}	ϕ_{22}	ϕ_{23}	ϕ_{24}	ϕ_{25}	ϕ_{31}	ϕ_{32}	ϕ_{33}	ϕ_{34}	ϕ_{35}
droop-1 [5], [6]	PI	0	0	0	0	0	P	0	0	0	0	0	0	P	0
droop-2 [11]	PI	0	0	0	0	0	0	0	P	0	0	I	0	0	I
droop-3 [6], [34]	PI	0	0	0	0	0	IF	0	0	0	0	0	0	0	0
droop-4 [14]	PI	0	0	0	0	0	PD	0	0	0	0	0	0	P	0
droop-5 [7]	PI	0	0	0	0	0	P{IF×D}	0	0	0	0	0	0	P	0
PSC-1 [6]	PI	0	0	0	0	0	P	0	0	0	0	0	0	P	0
PSC-2 [15]	PI	0	0	0	0	0	IF×PD	0	0	0	0	0	0	I	0
PSC-3 [16]	PI	0	0	0	0	0	IF×PD	0	0	0	0	0	0	I	0
VSG-1 [25], [35]	PI	0	0	0	0	0	IF	0	0	0	0	0	0	0	IF
VSG-2 [24], [25], [33]	PI	0	0	0	0	0	IF	0	0	0	0	0	0	PI	PI
VSG-3 [20]	PI	0	0	0	0	0	IF	0	0	0	0	0	P	P	0
VSG-4 [36]	PI	0	0	0	0	0	IF	IF	0	0	0	0	0	P	0
VSG-5 [7], [24], [37]	PI	0	0	0	0	0	IF	IF	0	0	0	0	0	PI	PI
VSG-6 [19]	PI	0	0	0	0	0	IF	0	0	IF	0	0	0	I	I
VSG-7 [18]	PI	0	0	0	0	0	O×PD	0	0	0	0	0	0	I	I
VSG-8 [7]	PI	0	0	0	0	0	IF×PD	0	0	0	0	0	0	PI	PI
VSG-9 [22]	PI	0	0	0	0	IF×PD	IF×PD	0	0	0	0	0	0	P	0
VSG-10 [24]	PI	0	0	0	0	0	$\text{IF}_1\{\text{IF}_1\times\text{IF}_2\times\text{D}\}$	0	0	0	0	0	0	PI	PI
VSG-11 [26]	PI	0	0	0	0	0	O×PD{O×IF×PD×D}	0	0	0	0	0	0	I	I
VSG-12 [23], [24]	PI	0	0	0	0	0	$\text{O}\times\text{PD}_1\{\text{O}\times\text{IF}\times\text{PD}_2\times\text{D}\}$	0	0	0	0	0	0	PI	PI
matching-1 [8]	P	0	0	0	0	P	0	0	0	0	0	0	0	0	PI
matching-2 [21]	0	0	0	0	0	P	0	0	0	0	P	0	0	0	0
Generated Inputs $\boldsymbol{u}$	i_u					ω_u					E_u				

P: Proportional controller k, I: Integral controller $\frac{1}{Ts}$, D: Derivative controller Ts, PI: Proportional integral controller $k(1+\frac{1}{Ts})$, PD: Proportional derivative controller $k(1+Ts)$, IF: Inertia factor $\frac{k}{Ts+1}$, O: Oscillatory factor $\frac{k}{T^2s^2+2T\xi s+1}$.
$\{\}$: the term is only applied to the feedback channel.

example, although PSC-2, PSC-3, and VSG-8 have distinctions from the original control blocks, and they are derived from different motivations, their frequency controls are actually identical. As another example, many works have proved the equivalence between droop-5 and VSG-2 in the frequency control [7], [28]. However, this is not entirely correct from Table I. When the disturbance is from the output side, e.g., p, the droop-5 is actually identical with VSG-2. However, if the disturbance is from the input side, e.g., P_{ref}, they are not identical. A similar analysis can be applied to study also other methods.

3) Different loops, i.e., DC control, active power control, and reactive power control of the grid-forming controls can be taken care of simultaneously to optimize the performance. Most of the existing grid-forming controls aim to decouple those control loops to simplify the design and analysis. However, note from Table I that some methods have successfully used some coupling terms to improve the performance.
4) New grid-forming controls can be inspired: In the proposed generalized configuration, the design of the grid-forming control is attributed to the control transfer matrix Φ. In the future, two directions can be pursued to propose new grid-forming controls. On the one hand, most of the used elements of the existing controls are linear. Nonlinear controllers such as sine function may be used especially to improve the global stability like in [10]. On the other hand, the control transfer matrix Φ of the existing controls are quite sparse and different coupling terms, e.g., the DC signals motivated from the matching control [38], can be added. In the following, we will present an example design.

It is worth to mention that the proposed generalized configuration can be further generalized in the following aspects.

1) This paper does not consider the virtual impedance and inner voltage and current loops, as they are not the essence of the grid-forming functions and not appear in some controls [7], [8], [18]. Nevertheless, they can be included by just adding their equations in $(\boldsymbol{f}, \boldsymbol{g})$ in Fig. 5. Moreover, the multivariable control design can be used to replace these SISO loops.
2) As mentioned before, the linear error $\boldsymbol{e} = \boldsymbol{Y}_{ref} - \boldsymbol{y}$ is a simple and natural choice. Nevertheless, other kinds of error signals can also be used, where, for example, $(v_{dcref}^2 - v_{dc}^2)/2$ is used in PSC in [39]. Furthermore, $P_{ref}/V_{ref}^2 - p/V^2$ and $Q_{ref}/V_{ref}^2 - q/V^2$ can be used as well, which is the case of dVOC [9]. Thus, by enlarging the available error signals, more kinds of grid-forming control can be unified into the proposed configuration.
3) The control transfer matrices of grid-forming controls summarized in Table I are all with fixed parameters. They can also be chosen as time-varying or functions of the angle of the (possibly estimated) grid impedance to encompass various kinds of adaptive control [40].

III. $\mathcal{H}_\infty$ Control Design of Grid-Forming Converter

The proposed generalized configuration considers the grid-forming converter as a MIMO system with a multivariable control transfer matrix ruling out traditional design and tuning methods for SISO systems. In this section, a new structured and multivariable control transfer matrix for the MIMO-GFM control is first proposed. Then we present how the design of the control transfer matrix can be transformed into a standard fixed-structure $\mathcal{H}_\infty$ optimization problem, where all control parameters can be tuned simultaneously.

A. Proposed Control Transfer Matrix

As mentioned before, the existing control transfer matrices are based on SISO loops and thus sparse. Therefore, our proposed control transfer matrix tries to improve the performance by adding some coupling terms. The following possible principles are considered in this paper.

1) ϕ_{11} is chosen as a PI controller to regulate v_{dc} with a zero steady-state error as

$$\phi_{11} = k_{pdc} + \frac{k_{idc}}{s}. \tag{32}$$

Nevertheless, the choice $k_{idc} = 0$ is possible, which is required for the matching controllers.

2) ϕ_{22} should provide some inertia for the frequency control and maintain the prescribed steady-state droop characteristics. We thus choose it as

$$\phi_{22} = \frac{D_p k_{22}}{s + k_{22}}. \tag{33}$$

3) A PLL (i.e., ω_g) is not expected to be used. Therefore the third column is chosen to be zero

$$\phi_{13} = \phi_{23} = \phi_{33} = 0. \tag{34}$$

This is just one option but others are possible if a PLL is available to improve the control performance.

4) The I control is used to keep the steady-state q-V droop characteristics as follows:

$$\phi_{34} = D_q \phi_{35} = \frac{k_{34}}{s}. \tag{35}$$

5) The coupling terms of q and V on the frequency control should not change the steady-state p-f droop characteristics. Therefore, the following elements are chosen

$$\phi_{24} = D_q \phi_{25} = k_{24} \tag{36}$$

6) All the other elements are chosen, for simplicity, as P controllers to be designed.

Overall, the proposed control transfer matrix for the MIMO-GFM takes the following form:

$$\boldsymbol{\Phi} = \begin{bmatrix} k_{pdc} + k_{idc}/s & k_{12} & 0 & k_{14} & k_{15} \\ k_{21} & D_p k_{22}/(s + k_{22}) & 0 & k_{24} & k_{24}/D_q \\ k_{31} & k_{32} & 0 & k_{34}/s & \frac{k_{34}/D_q}{s} \end{bmatrix}, \tag{37}$$

where the block diagram is shown in Fig. 10. Observed that, unlike previously proposed variations and improved methods,

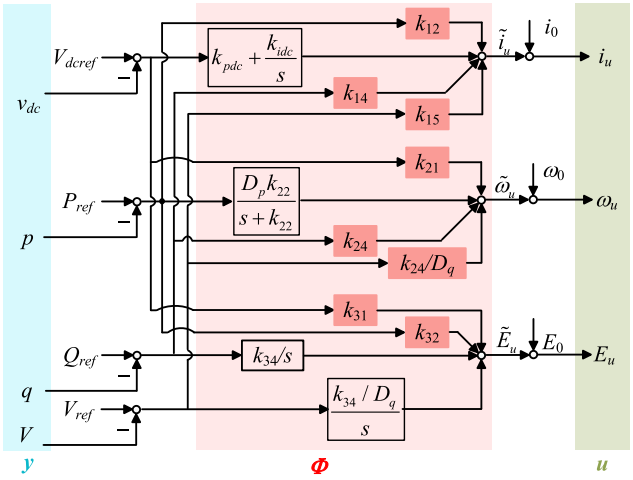

Fig. 10. Block diagram of proposed MIMO-GFM control.

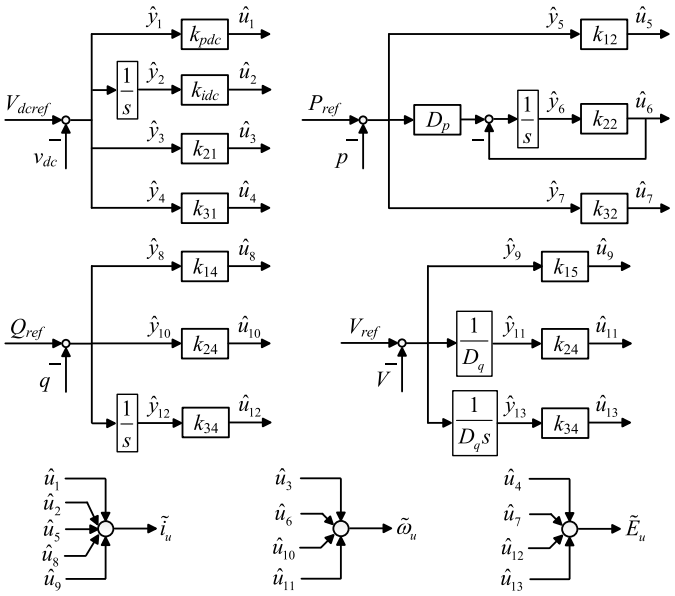

Fig. 11. Block diagram of used control transfer matrix.

the order of the proposed control transfer matrix $\boldsymbol{\Phi}$ is not increased compared to the basic droop control with LPFs and VSG, since the added coupling terms are all P controllers. The above shows one reasonable choice for Φ. Other choices are possible as well.

B. Parameters Design Based on $\mathcal{H}_\infty$ Optimization

1) Formulation of $\mathcal{H}_\infty$ Synthesis: In order to transform the control parameter design into a standard $\mathcal{H}_\infty$ optimization problem, the parameters to be selected are separated by defining two intermediate vectors $\hat{\boldsymbol{u}}$ and $\hat{\boldsymbol{y}}$ as shown in Fig. 11. Thus, there is the following relationship

$$\begin{aligned} \hat{\boldsymbol{u}} &= diag\big(k_{pdc}, k_{idc}, k_{21}, k_{31}, k_{12}, k_{22}, k_{32}, k_{14}, k_{15}, k_{24}\boldsymbol{I_2}, k_{34}\boldsymbol{I_2}\big)\hat{\boldsymbol{y}} \\ &= \boldsymbol{K}\hat{\boldsymbol{y}}. \end{aligned} \tag{38}$$

It is observed that all the parameters to be designed are included in the static gain $\boldsymbol{K}$. Thereafter, the standard structure

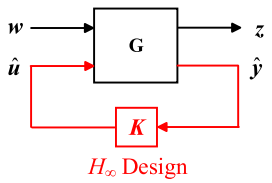

Fig. 12. Block diagram of grid-forming converter in LFT.

in the so-called linear fractional transformation (LFT) for $\mathcal{H}_\infty$ synthesis can be derived as in Fig. 12, where the system in Fig. 5 is collapsed into **G** (except for $\boldsymbol{K}$). Meanwhile, $\boldsymbol{w}$ and $\boldsymbol{z}$ are defined disturbance inputs and performance outputs for the $\mathcal{H}_\infty$ synthesis. In this paper, they are chosen as

$$\boldsymbol{w} = \begin{bmatrix} P_{ref} & \omega_g \end{bmatrix}^T \tag{39}$$

$$\boldsymbol{z} = \begin{bmatrix} P_{ref} - p & p & \omega_u & q + V/D_q \end{bmatrix}^T. \tag{40}$$

2) Choices of Weighting Functions: The $\mathcal{H}_\infty$ optimization uses some weighting functions to limit the disturbance responses from $\boldsymbol{w}$ to $\boldsymbol{z}$. Let $T_{ij}(s)$ be the transfer function from w_j to z_i and $W_{ij}(s)$ be the corresponding weighting function. In this paper, the following weightings $W_{ij}(s)$ are selected.

To have a small active power tracking error, low-frequency gain of $T_{11}(s)$ should be small. Therefore, $W_{11}(s)$ is chosen as:

$$W_{11}(s) = \frac{s + s_{11\_1}}{s + s_{11\_2}}. \tag{41}$$

To limit the high-frequency disturbance to the active power, high-frequency gain of $T_{21}(s)$ and $T_{22}(s)$ should rapidly decay. Therefore, $W_{21}(s)$ and $W_{22}(s)$ are chosen as:

$$W_{21}(s) = \left(\frac{T_{21\_1}s + 1}{T_{21\_2}s + 1}\right)^2 \tag{42}$$

$$W_{22}(s) = \frac{1}{k_{w22}} \times \frac{T_{22\_1}s + 1}{T_{22\_2}s + 1}. \tag{43}$$

Meanwhile, the frequency of the grid-forming converter ω_u should not vary quickly as a response to $\boldsymbol{w}$. Therefore, the following weights $W_{31}(s)$ and $W_{32}(s)$ are chosen to limit the high-frequency gain of $T_{31}(s)$ and $T_{32}(s)$:

$$W_{31}(s) = \frac{1}{k_{w31}} \times \frac{s}{T_{31\_2}s + 1} \tag{44}$$

$$W_{32}(s) = \frac{T_{32\_1}s + 1}{T_{32\_2}s + 1}. \tag{45}$$

Last, as mentioned before, the control of ω_u should not influence the steady-state q-V droop regulation. Therefore, $W_{41}(s)$ is used to limit the low-frequency gain of $T_{41}(s)$ as

$$W_{41} = \frac{s + s_{41\_1}}{s + s_{41\_2}}. \tag{46}$$

The used numbers in the weighting functions are summarized in Table II, which are chosen depending on the converter parameters like shown in Table III.

The log-magnitude curves of the used $W_{ij}(s)$ are shown in Fig. 13. Afterwards, the gain vector $\boldsymbol{K}$ can be derived by solving (e.g., via MATLAB's instructor *hinfstruct* [41])

$$\min_{\boldsymbol{K}} \left\| diag\left(W_{ij}(s)T_{ij}(s)\right) \right\|_\infty \tag{47}$$

TABLE II
NUMBERS USED IN WEIGHTING FUNCTIONS

Symbol	Value	Symbol	Value
s_{11_1}	4	s_{11_2}	0.0004
T_{21_1}	1.447×10^{-3}	T_{21_2}	1.447×10^{-5}
k_{w22}	100	T_{22_1}	1.447×10^{-3}
T_{22_2}	1.447×10^{-5}	k_{w31}	0.015
T_{31_2}	1.447×10^{-5}	T_{32_1}	1.447×10^{-3}
T_{32_2}	1.447×10^{-5}	s_{41_1}	60
s_{41_2}	0.006		

TABLE III
PARAMETERS USED IN SIMULATIONS

Symbol	Description	Value
ω_n	nominal frequency	100π rad/s
S_n	nominal power	4 kW
V_n	nominal line-to-line RMS voltage	380 V
ω_g	grid frequency	1 p.u.
V_g	grid voltage	1 p.u.
L_g	line inductor	2 mH
R_g	line resistor	0.06 Ω
C_f	filter capacitor	20 μF
L_f	filter inductor	2 mH
R_f	filter resistor	0.06 Ω
C_{dc}	DC capacitor	500 μF
D_p	droop coefficient of P-f regulation	0.01 p.u.
D_q	droop coefficient of Q-V regulation	0.05 p.u.
P_{ref}	Active power reference	0.5 p.u.
Q_{ref}	Reactive power reference	0 p.u.
V_{ref}	Voltage magnitude reference	1 p.u.
V_{dcref}	DC voltage reference	700 V

which, with the parameters listed in Table III and the initial values $\boldsymbol{K} = diag(90, 400, 0, 0, 0, 20, 0, 0, 0, 0, 0, 1, 1)$, yields

$$\boldsymbol{\Phi} = \begin{bmatrix} 120.224 + \frac{265.6217}{s} & -0.0019 & 0 & 0.1673 & -0.8274 \\ -0.8382 & \frac{0.017622}{s+1.7622} & 0 & 0 & 0 \\ -4.8977 & 0 & 0 & \frac{1.0844}{s} & \frac{21.6872}{s} \end{bmatrix}. \tag{48}$$

By setting the coupling terms to be zeros, (48) becomes

$$\boldsymbol{\Phi} = \begin{bmatrix} 120.224 + \frac{265.6217}{s} & 0 & 0 & 0 & 0 \\ 0 & \frac{0.017622}{s+1.7622} & 0 & 0 & 0 \\ 0 & 0 & 0 & \frac{1.0844}{s} & \frac{21.6872}{s} \end{bmatrix}. \tag{49}$$

To highlight the effects of the coupling terms, Fig. 14 shows the changes of the system's eigenvalues with (i.e., using (48)) and without (i.e., using (49)) these coupling terms. As shown, the coupling terms increase the damping ratio of the oscillation modes. Especially, the damping ratios of the mode with the synchronous frequency and the dominant low-frequency mode are highly increased from less than 0.1 to more than

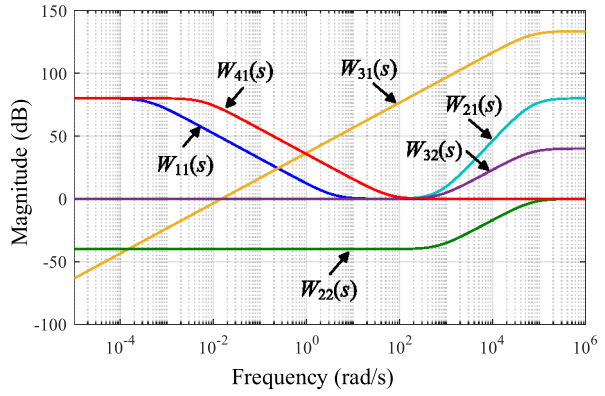

Fig. 13. Log-magnitude curves of used weighting functions.

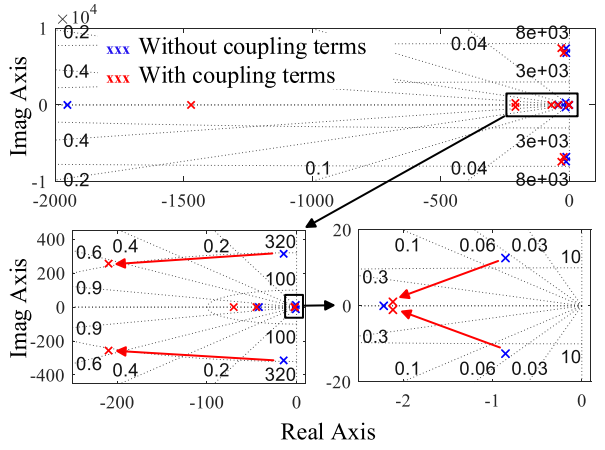

Fig. 14. Eigenvalues of the system with and without coupling terms.

0.6. Therefore, the dynamics of the system will be significantly improved with the coupling terms. All of this is of course to be expected from an optimization perspective. The controller architecture underlying (48) includes (49) and it is designed to be optimal with respect to the $\mathcal{H}_\infty$ criterion. Thus, inevitably, the optimal design resulting in (48) will outperform (49), which is suboptimal and results in poorer performance.

C. Generalized Parameters Design Procedure

Although the above section shows a specific case, the proposed $\mathcal{H}_\infty$-based parameters design method can be generalized to any grid-forming converter controllers. The design procedure can be summarized as follows.

1) Establish the model of a grid-forming converter in the form of the general configuration shown in Fig. 5.
2) Separate the designed parameters by defining intermediate vectors (like the way shown in Fig. 11 and (38)).
3) Choose the disturbance inputs and performance outputs (e.g., (39) and (40)).
4) Transform the established model in step 1) into the standard LFT shown in Fig. 12.
5) Choose weighting functions for the focused transfer functions from inputs to outputs chosen in Step 3) (e.g., (41)-(46)).

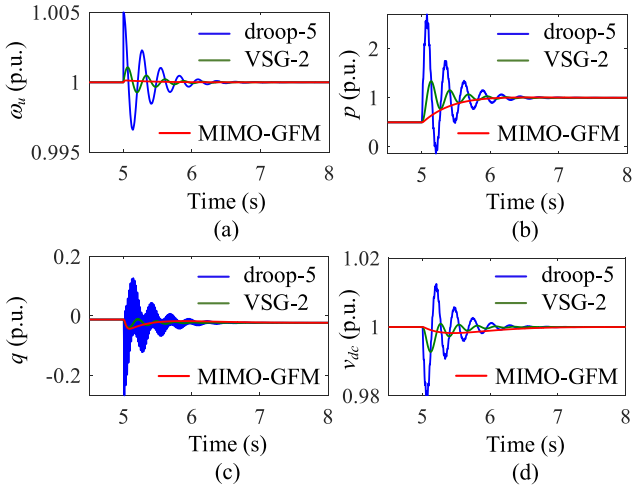

Fig. 15. Simulation comparisons among different grid-forming converters when P_{ref} steps from 0.5 p.u. to 1 p.u.

6) Solve the $\mathcal{H}_\infty$ optimization problem of (47) to obtain the values of the designed parameters.

IV. Simulation and Experimental Results

A. Simulation Results

To present the advantages of the proposed MIMO-GFM converter, the time-domain simulations results carried out by MATLAB/Simulink are provided, where the topology is the same as in Fig. 1, and the parameters are listed in Table III.

To show the benefits of the added coupling terms, the VSG-2 and droop-5 controls in Table I are used for comparison. The sparse control transfer matrix of VSG-2 is also designed by the same optimization routine as in (47) as

$$\mathbf{\Phi} = \begin{bmatrix} 90 + \frac{400}{s} & 0 & 0 & 0 & 0 \\ 0 & \frac{0.059801}{s+5.9801} & 0 & 0 & 0 \\ 0 & 0 & 0 & \frac{1.9048}{s} & \frac{38.0954}{s} \end{bmatrix}. \quad (50)$$

Meanwhile, the parameters of droop-5 are designed by its equivalent relationship with VSG-2 as shown in [7] and [28].

Fig. 15 presents the simulation comparisons when P_{ref} steps from 0.5 p.u. to 1 p.u. As it is seen, both the droop-5 control and the VSG-2 control show larger oscillations responding to the disturbance. On the contrary, the proposed MIMO-GFM control can well damp this oscillation and has much smoother dynamics. It is also observed that the droop-5 control and the VSG-2 control have different response because P_{ref} is seen as a disturbance at the input side as mentioned before.

Fig. 16 presents simulation comparisons when ω_g decreases from 50 Hz to 49.9 Hz. As seen, the frequency of the proposed MIMO-GFM converter can synchronize to the power grid quickly and smoothly with almost no overshoot. In comparison, the droop-5 control and the VSG-2 control will lead to larger oscillations. It also shows the equivalence between the droop-5 control and the VSG-2 control in this case as ω_g is seen as a disturbance at the output side.

The dynamics responding to a grid voltage drop of 0.01 p.u. are also compared as shown in Fig. 17. As seen,

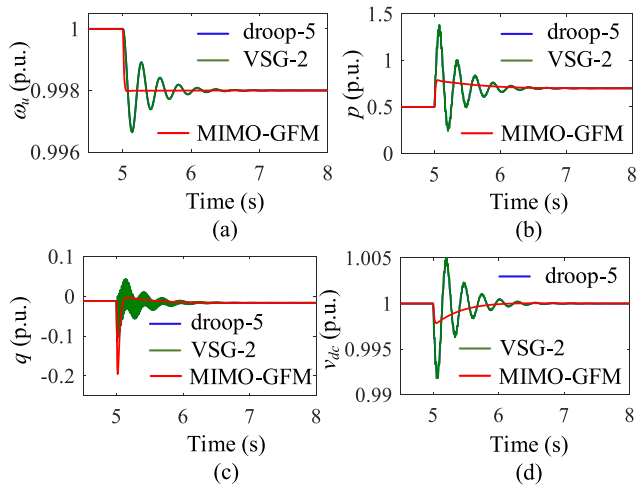

Fig. 16. Simulation comparisons among different grid-forming converters when grid frequency decreases from 50 Hz to 49.9 Hz.

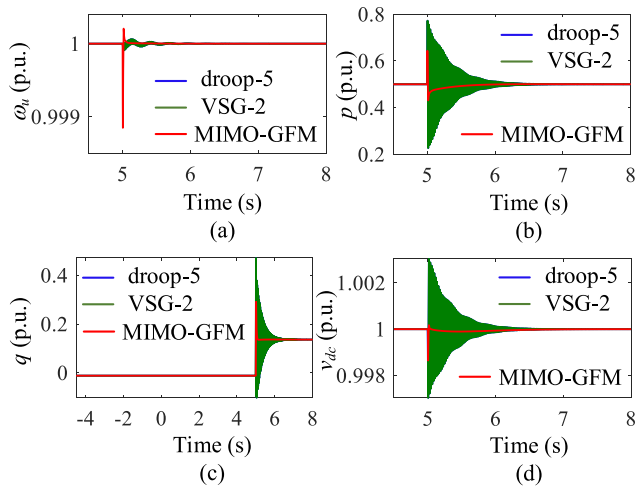

Fig. 17. Simulation comparisons among different grid-forming converters when grid voltage decreases from 1 p.u. to 0.99 p.u.

the oscillations with proposed MIMO-GFM control can be damped quickly. In comparison, the droop-5 control and the VSG-2 control will lead to large oscillations, especially with the synchronous frequency. It should be mentioned that the performance of the MIMO-GFM control can be further improved by adding V_g in (39) when necessary.

B. Experimental Results

To further validate the effectiveness of the proposed MIMO-GFM control, an experimental setup is established, as shown in Fig. 18. The power stage consists of a Danfoss drives system, an LCL filter and a Chroma 61845 grid simulator, while the control is implemented by the DS1007 dSPACE system. Meanwhile, the DS2004 A/D board and DS2101 D/A board are used to do measurement and generate the output, respectively. It should be mentioned that, because the DC control is fixed in the DC source provided by a Yaskawa D1000 regenerative converter, the first row of the control transfer matrix corresponding to the DC voltage control is not a design variable in the experiments. It should be mentioned that the DC

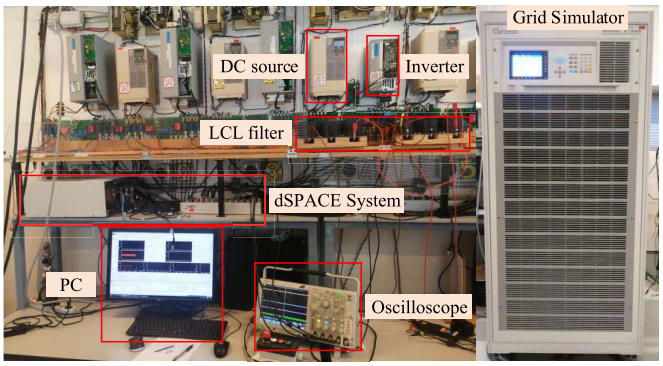

Fig. 18. Experimental setup.

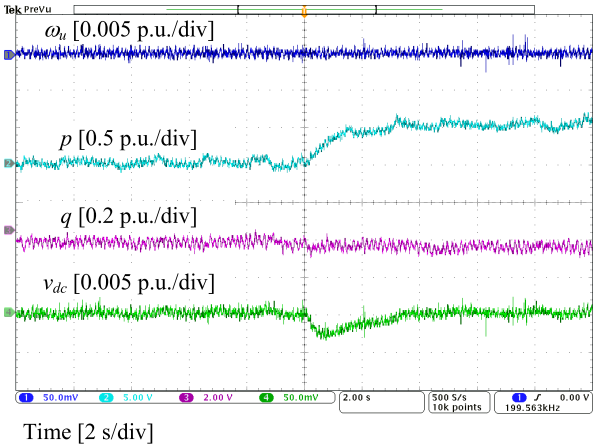

Fig. 19. Experimental results of the proposed MIMO-GFM controller when P_{ref} steps from 0.5 p.u. to 1 p.u.

voltage from the Yaskawa D1000 regenerative converter is not strictly constant in steady-state but with some fluctuations, which will inevitably lead to fluctuations in other variables in steady-state due to the couplings in the MIMO-GFM converter. Nevertheless, these fluctuations are independent of the proposed control, and we can still show the functions of the coupling terms in the frequency and voltage control in the second and third rows. The parameters of the setup are identical with Table III.

Figs. 19–21 show the experimental results with the proposed MIMO-GFM control responding to the changes of P_{ref}, ω_g, and V_g respectively. As shown, the dynamics are fast and smooth with almost no oscillations, which validates a good performance of the proposed method. It should be mentioned that the traditional VSG control cannot be stabilized in the experiments, as shown in Fig. 22, due to various disturbances such as parameter errors and delays in the physically experimental system, although its oscillations can be damped in the simulations. This further highlights the robustness of the proposed method.

C. Discussion on Results

According to Table III, the short-circuit ratio (SCR) of the grid is 28.5, which implies a quite strong grid. Therefore, the poor dynamics of VSG-2 and droop-5 in Fig. 15 and

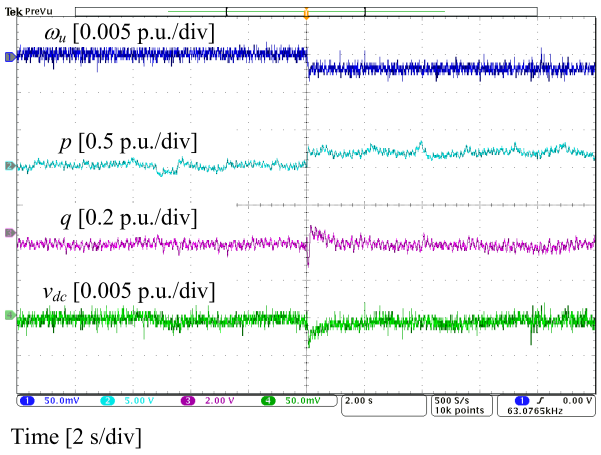

Fig. 20. Experimental results of the proposed MIMO-GFM controller when grid frequency decreases from 50 Hz to 49.9 Hz.

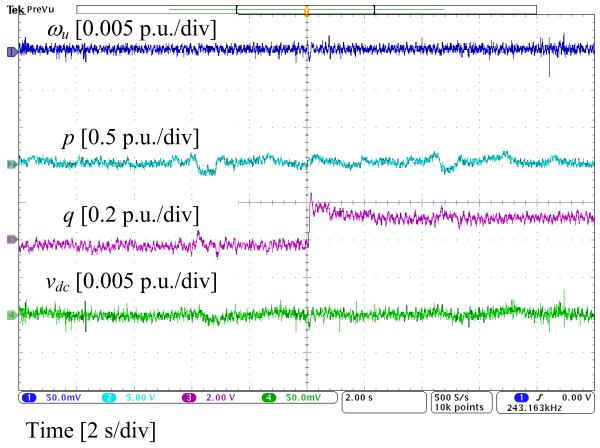

Fig. 21. Experimental results of the proposed MIMO-GFM controller when grid voltage decreases from 1 p.u. to 0.99 p.u.

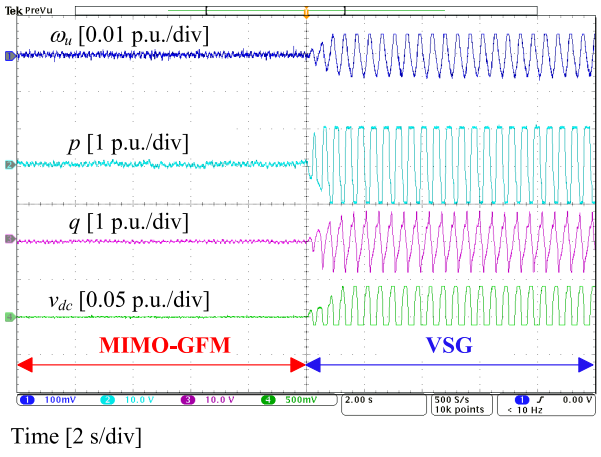

Fig. 22. Experimental results when control strategy is switched from MIMO-GFM to VSG-2.

Fig. 16 are to be expected. Namely, it has been shown that these kinds of grid-forming controllers are suitable for weak grids, but may lead to poor stability in strong grids due to the fact that grid-forming converters behave like a voltage

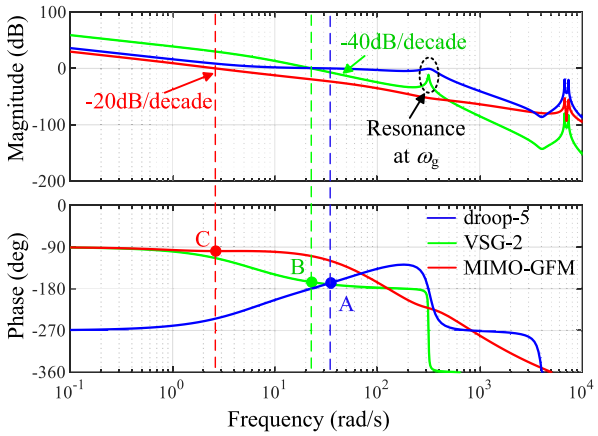

Fig. 23. Open-loop bode diagram of different grid-forming controllers.

source [42], [43]. It will be harder for the grid-forming converters to regulate the voltage at the point of common coupling (PCC) in a stronger grid [43]. Therefore, those basic grid-forming controllers may not provide good performance. This can also be proved from the open-loop bode diagram as shown in Fig. 23. When connected to this strong grid, both the droop-5 and VSG-2 controllers lead to quite small phase margins (PMs) of 12.8° and 14.3° at point A and point B, respectively. Further taking the VSG-2 as an example, this small PM is because the slope of the log-magnitude curve at the gain crossover frequency is −40 dB/decade. These small PMs are unacceptable in practice (PM $\geq$ 30° is usually required) due to the fact that small errors between the ideal and actual models will cause instability, as shown in the experimental results of Fig. 22. This kind of instability for the VSG has also been pointed out in [44]. Among the previous research approaches, several methods have been used to overcome this problem such as setting a large line impedance [6], [7], [20] or virtual impedance [15], [17], [27], [44] to decrease the SCR (e.g., less than 10), and using improved high-order forms as in Table I. In comparison, the proposed MIMO-GFM controller has enough PM at point C (shown in Fig. 23) to easily accommodate model uncertainties.

The other problem of the traditional controllers is the synchronous resonance due to the inductive line, which can also be observed in Fig. 23. A detailed analysis is reported in [44]–[46].

Both the simulations and experimental results validate that the proposed MIMO-GFM controller can well solve all the aforementioned problems, and it admits a superior and robust performance without changing the SCR or applying high-order forms.

V. Conclusion

This paper proposes a generalized configuration for the grid-forming converter based on multi-input-multi-output feedback control theory. Instead of assuming that different loops are decoupled, the proposed configuration considers DC voltage control, frequency control, and voltage control as a single MIMO control transfer matrix to be designed. It is shown that many of the popular grid-forming controls as well as their

improved formulations can be unified into a generalized control transfer matrix in the proposed configuration. Besides, this configuration is also helpful in comparison and design of controls. We also proposed a new MIMO-GFM control without increasing the order of the controller. To cope with the multiple control parameters, this paper presents how the optimal control design can be transformed to a standard $\mathcal{H}_\infty$ optimization problem. The simulation and experimental results verify the superior performance of the proposed method.

REFERENCES

[1] I. Colak, E. Kabalci, G. Fulli, and S. Lazarou, "A survey on the contributions of power electronics to smart grid systems," *Renew. Sustain. Energy Rev.*, vol. 47, no. 1, pp. 562–579, Jul. 2015.

[2] B. K. Bose, "Power electronics, smart grid, and renewable energy systems," *Proc. IEEE*, vol. 105, no. 11, pp. 2011–2018, Nov. 2017.

[3] M. G. Molina, "Energy storage and power electronics technologies: A strong combination to empower the transformation to the smart grid," *Proc. IEEE*, vol. 105, no. 11, pp. 2191–2219, Nov. 2017.

[4] F. Milano, F. Dörfler, G. Hug, D. J. Hill, and G. Verbic, "Foundations and challenges of low-inertia systems," in *Proc. Power Syst. Comput. Conf.*, 2018, pp. 1–25.

[5] J. Rocabert, A. Luna, F. Blaabjerg, and P. Rodríguez, "Control of power converters in AC microgrids," *IEEE Trans. Power Electron.*, vol. 27, no. 11, pp. 4734–4749, Nov. 2012.

[6] D. Pan, X. Wang, F. Liu, and R. Shi, "Transient stability of voltage-source converters with grid-forming control: A design-oriented study," *IEEE J. Emerg. Sel. Topics Power Electron.*, vol. 8, no. 2, pp. 1019–1033, Jun. 2020.

[7] J. Liu, Y. Miura, and T. Ise, "Comparison of dynamic characteristics between virtual synchronous generator and droop control in inverter-based distributed generators," *IEEE Trans. Power Electron.*, vol. 31, no. 5, pp. 3600–3611, May 2016.

[8] C. Arghir, T. Jouini, and F. Dörfler, "Grid-forming control for power converters based on matching of synchronous machines," *Automatica*, vol. 95, pp. 273–282, Sep. 2018.

[9] A. Tayyebi, D. Groß, A. Anta, F. Kupzog, and F. Dörfler, "Frequency stability of synchronous machines and grid-forming power converters," *IEEE J. Emerg. Sel. Topics Power Electron.*, vol. 8, no. 2, pp. 1004–1018, Jun. 2020.

[10] A. Tayyebi, A. Anta, and F. Dörfler, "Hybrid angle control and almost global stability of grid-forming power converters," 2020, *arXiv:2008.07661*.

[11] Q.-C. Zhong, "Robust droop controller for accurate proportional load sharing among inverters operated in parallel," *IEEE Trans. Ind. Electron.*, vol. 60, no. 4, pp. 1281–1290, Apr. 2013.

[12] Z. Peng, J. Wang, D. Bi, Y. Dai, and Y. Wen, "The application of microgrids based on droop control with coupling compensation and inertia," *IEEE Trans. Sustain. Energy*, vol. 9, no. 3, pp. 1157–1168, Jul. 2018.

[13] X. Meng, J. Liu, and Z. Liu, "A generalized droop control for grid-supporting inverter based on comparison between traditional droop control and virtual synchronous generator control," *IEEE Trans. Power Electron.*, vol. 34, no. 6, pp. 5416–5438, Jun. 2019.

[14] J. C. Vasquez, J. M. Guerrero, M. Savaghebi, J. Eloy-Garcia, and R. Teodorescu, "Modeling, analysis, and design of stationary-reference-frame droop-controlled parallel three-phase voltage source inverters," *IEEE Trans. Ind. Electron.*, vol. 60, no. 4, pp. 1271–1280, Apr. 2013.

[15] W. Zhang, D. Remon, and P. Rodriguez, "Frequency support characteristics of grid-interactive power converters based on the synchronous power controller," *IET Renew. Power Gener.*, vol. 11, no. 4, pp. 470–479, Mar. 2017.

[16] X. Quan, A. Q. Huang, and H. Yu, "A novel order reduced synchronous power control for grid-forming inverters," *IEEE Trans. Ind. Electron.*, vol. 67, no. 12, pp. 10989–10995, Dec. 2020.

[17] O. Mo, S. D'Arco, and J. A. Suul, "Evaluation of virtual synchronous machines with dynamic or quasi-stationary machine models," *IEEE Trans. Ind. Electron.*, vol. 64, no. 7, pp. 5952–5962, Jul. 2017.

[18] Z. Shuai, W. Huang, Z. J. Shen, A. Luo, and Z. Tian, "Active power oscillation and suppression techniques between two parallel synchronverters during load fluctuations," *IEEE Trans. Power Electron.*, vol. 35, no. 4, pp. 4127–4142, Apr. 2020.

[19] Z. Shuai, C. Shen, X. Liu, Z. Li, and Z. J. Shen, "Transient angle stability of virtual synchronous generators using Lyapunov's direct method," *IEEE Trans. Smart Grid*, vol. 10, no. 4, pp. 4648–4661, Jul. 2019.

[20] X. Xiong, C. Wu, and F. Blaabjerg, "An improved synchronization stability method of virtual synchronous generators based on frequency feedforward on reactive power control loop," *IEEE Trans. Power Electron.*, vol. 36, no. 8, pp. 9136–9148, Aug. 2021.

[21] Y. Li, X. Yuan, J. Li, H. Xiao, Z. Xu, and Z. Du, "Novel grid-forming control of PMSG-based wind turbine for integrating weak AC grid without sacrificing maximum power point tracking," *IET Gener. Transm. Distrib.*, vol. 15, no. 10, pp. 1613–1625, May 2021.

[22] L. Huang, H. Xin, H. Yang, Z. Wang, and H. Xie, "Interconnecting very weak AC systems by multiterminal VSC-HVDC links with a unified virtual synchronous control," *IEEE J. Emerg. Sel. Topics Power Electron.*, vol. 6, no. 3, pp. 1041–1053, Sep. 2018.

[23] J. Liu, Y. Miura, and T. Ise, "Fixed-parameter damping methods of virtual synchronous generator control using state feedback," *IEEE Access*, vol. 7, pp. 99177–99190, 2019.

[24] J. Liu, Y. Miura, H. Bevrani, and T. Ise, "A unified modeling method of virtual synchronous generator for multi-operation-mode analyses," *IEEE J. Emerg. Sel. Topics Power Electron.*, vol. 9, no. 2, pp. 2394–2409, Apr. 2021.

[25] M. Chen, D. Zhou, and F. Blaabjerg, "Voltage control impact on performance of virtual synchronous generator," in *Proc. IEEE 12th Energy Convers. Congr. Expo. Asia*, 2021, pp. 1981–1986.

[26] M. Chen, D. Zhou, and F. Blaabjerg, "Active power oscillation damping based on acceleration control in paralleled virtual synchronous generators system," *IEEE Trans. Power Electron.*, vol. 36, no. 8, pp. 9501–9510, Aug. 2021.

[27] L. Huang, H. Xin, and F. Dörfler, "H_∞-control of grid-connected converters: Design, objectives and decentralized stability certificates," *IEEE Trans. Smart Grid*, vol. 11, no. 5, pp. 3805–3816, Sep. 2020.

[28] S. D'Arco and J. A. Suul, "Equivalence of virtual synchronous machines and frequency-droops for converter-based microgrids," *IEEE Trans. Smart Grid*, vol. 5, no. 1, pp. 394–395, Jan. 2014.

[29] R. Rosso, X. Wang, M. Liserre, X. Lu, and S. Engelken, "Grid-forming converters: Control approaches, grid-synchronization, and future trends—A review," *IEEE Open J. Ind. Appl.*, vol. 2, pp. 93–109, 2021.

[30] R. Rosso, J. Cassoli, G. Buticchi, S. Engelken, and M. Liserre, "Robust stability analysis of LCL filter based synchronverter under different grid conditions," *IEEE Trans. Power Electron.*, vol. 34, no. 6, pp. 5842–5853, Jun. 2019.

[31] A. Fathi, Q. Shafiee, and H. Bevrani, "Robust frequency control of microgrids using an extended virtual synchronous generator," *IEEE Trans. Power Syst.*, vol. 33, no. 6, pp. 6289–6297, Nov. 2018.

[32] C. Kammer, S. D'Arco, A. G. Endegnanew, and A. Karimi, "Convex optimization-based control design for parallel grid-connected inverters," *IEEE Trans. Power Electron.*, vol. 34, no. 7, pp. 6048–6061, Jul. 2019.

[33] A. Rodriguez-Cabero, J. Roldán-Pérez, and M. Prodanovic, "Virtual impedance design considerations for virtual synchronous machines in weak grids," *IEEE J. Emerg. Sel. Topics Power Electron.*, vol. 8, no. 2, pp. 1477–1489, Jun. 2020.

[34] X. Fu *et al.*, "Large-signal stability of grid-forming and grid-following controls in voltage source converter: A comparative study," *IEEE Trans. Power Electron.*, vol. 36, no. 7, pp. 7832–7840, Jul. 2021.

[35] M. Chen, D. Zhou, and F. Blaabjerg, "Characteristics of virtual synchronous generator based voltage source converter," in *Proc. IEEE Power Energy Soc. Gen. Meeting*, 2020, pp. 1–5.

[36] X. Xiong, C. Wu, B. Hu, D. Pan, and F. Blaabjerg, "Transient damping method for improving the synchronization stability of virtual synchronous generators," *IEEE Trans. Power Electron.*, vol. 36, no. 7, pp. 7820–7831, Jul. 2021.

[37] H. Cheng, Z. Shuai, C. Shen, X. Liu, Z. Li, and Z. J. Shen, "Transient angle stability of paralleled synchronous and virtual synchronous generators in islanded microgrids," *IEEE Trans. Power Electron.*, vol. 35, no. 8, pp. 8751–8765, Aug. 2020.

[38] S. Samanta and N. R. Chaudhuri, "On stability analysis of power grids with synchronous generators and grid-forming converters under DC-side current limitation," 2021, *arXiv:2103.09966*.

[39] L. Zhang, L. Harnefors, and H.-P. Nee, "Power-synchronization control of grid-connected voltage-source converters," *IEEE Trans. Power Syst.*, vol. 25, no. 2, pp. 809–820, May 2010.

[40] J. C. Vasquez, J. M. Guerrero, A. Luna, P. Rodriguez, and R. Teodorescu, "Adaptive droop control applied to voltage-source inverters operating in grid-connected and islanded modes," *IEEE Trans. Ind. Electron.*, vol. 56, no. 10, pp. 4088–4096, Oct. 2009.

[41] P. Gahinet and P. Apkarian, "Structured H_∞ synthesis in MATLAB," *IFAC Proc. Vol.*, vol. 44, no. 1, pp. 1435–1440, Jan. 2011.
[42] X. Wang, M. G. Taul, H. Wu, Y. Liao, F. Blaabjerg, and L. Harnefors, "Grid-synchronization stability of converter-based resources—An overview," *IEEE Open J. Ind. Appl.*, vol. 1, pp. 115–134, 2020.
[43] H. Zhang, W. Xiang, W. Lin, and J. Wen, "Grid forming converters in renewable energy sources dominated power grid: Control strategy, stability, application, and challenges," *J. Mod. Power Syst. Clean Energy*, vol. 9, no. 6, pp. 1239–1256, Nov. 2021.
[44] J. Chen and T. O'Donnell, "Parameter constraints for virtual synchronous generator considering stability," *IEEE Trans. Power Syst.*, vol. 34, no. 3, pp. 2479–2481, May 2019.
[45] J. Wang, Y. Wang, Y. Gu, W. Li, and X. He, "Synchronous frequency resonance of virtual synchronous generators and damping control," in *Proc. 9th Int. Conf. Power Electron. ECCE Asia (ICPE-ECCE Asia)*, 2015, pp. 1011–1016.
[46] D. Yang, H. Wu, X. Wang, and F. Blaabjerg, "Suppression of synchronous resonance for VSGs," *J. Eng.*, vol. 2017, no. 13, pp. 2574–2579, Jan. 2017.

Meng Chen (Member, IEEE) received the B.Eng. degree in electrical engineering and automation from the Qingdao University of Science and Technology, Qingdao, China, in 2013, the first Ph.D. degree in power system and automation from North China Electric Power University, Beijing, China, in 2018, and the second Ph.D. degree in energy technology from Aalborg University, Aalborg, Denmark, in 2022. He was a visiting scholar with Swiss Federal Institute of Technology (ETH) Zurich, Zurich, Switzerland, in 2021. Since 2022, he has been with Aalborg University, where he is currently a Postdoctoral Researcher. His research interest is the control, stability, and reliability of power systems with power electronics. He is a recipient of the 2020 MPCE Best Paper Award.

Dao Zhou (Senior Member, IEEE) received the B.S. degree in electrical engineering from Beijing Jiaotong University, Beijing, China, in 2007, the M.S. degree in electrical engineering from Zhejiang University, Hangzhou, China, in 2010, and the Ph.D. degree in electrical engineering from Aalborg University, Aalborg, Denmark, in 2014. Since 2014, he has been with Department of Energy Technology, Aalborg University, where currently he is an Associate Professor. His research interests include modeling, control, and reliability of power electronics in renewable energy applications. He also received a few IEEE prized paper awards. He serves as an Associate Editor for *IET Renewable Power Generation* and *IET Power Electronics*.

Ali Tayyebi received the B.Sc. degree in electrical engineering from the University of Tehran, Iran, in 2012, the first M.Sc. degree in engineering mathematics (joint MATHMODS Program) from the University of L'Aquila, Italy, and the University of Hamburg, Germany, in 2014, and the second M.Sc. degree in sustainable transportation and electric power systems (joint STEPS program) from the La Sapienza, Italy, University of Nottingham, U.K., and University of Oviedo, Spain, in 2016.

In 2016, he joined the Austrian Institute of Technology (AIT), Vienna, Austria, as a master thesis candidate and afterward continued with AIT as a Research Assistant. In 2017, he started his joint Ph.D. project with AIT and Automatic Control Laboratory, Swiss Federal Institute of Technology (ETH) Zurich, Switzerland. In 2022, he joined Hitachi Energy Research, Sweden. His main research interest is the non-linear systems and control theory with applications to power electronics/systems. His Ph.D. research focuses on the design of grid-forming converter control algorithms for low-inertia and hybrid AC/DC power grids.

Mr. Tayyebi was a recipient of the IEEE PES General Meeting 2020 Best Paper Award. From 2014 to 2016, he was a recipient of the EU Scholarship for master's studies.

Eduardo Prieto-Araujo (Senior Member, IEEE) received the degree in industrial engineering from the School of Industrial Engineering of Barcelona (ETSEIB), Technical University of Catalonia (UPC), Barcelona, Spain, in 2011, and the Ph.D. degree in electrical engineering from the UPC in 2016. He joined the CITCEA-UPC Research Group in 2010, and he is currently a Serra Húnter Lecturer with the Electrical Engineering Department, UPC. In 2021, he was a Visiting Professor with the Automatic Control Laboratory, ETH Zürich. His research interests include renewable generation systems, control of power converters for HVDC applications, interaction analysis between converters, and power electronics dominated power systems.

Florian Dörfler (Senior Member, IEEE) received the Diploma degree in engineering cybernetics from the University of Stuttgart in 2008, and the Ph.D. degree in mechanical engineering from the University of California at Santa Barbara in 2013. He is an Associate Professor with the Automatic Control Laboratory, ETH Zürich, and the Associate Head of the Department of Information Technology and Electrical Engineering. From 2013 to 2014, he was an Assistant Professor with the University of California at Los Angeles. His primary research interests are centered around control, optimization, and system theory with applications in network systems, in particular electric power grids. He is a recipient of the distinguished young research awards by IFAC (the Manfred Thoma Medal 2020) and EUCA (the European Control Award 2020). His students were winners or finalists for Best Student Paper awards at the European Control Conference in 2013 and 2019, the American Control Conference in 2016, the Conference on Decision and Control in 2020, the PES General Meeting in 2020, the PES PowerTech Conference in 2017, and the International Conference on Intelligent Transportation Systems in 2021. He is furthermore a recipient of the 2010 ACC Student Best Paper Award, the 2011 O. Hugo Schuck Best Paper Award, the 2012–2014 Automatica Best Paper Award, the 2016 IEEE Circuits and Systems Guillemin–Cauer Best Paper Award, and the 2015 UCSB ME Best Ph.D. Award.

Frede Blaabjerg (Fellow, IEEE) received the Ph.D. degree in electrical engineering from Aalborg University in 1995.

He was with ABB-Scandia, Randers, Denmark, from 1987 to 1988. He became an Assistant Professor, an Associate Professor, and a Full Professor of Power Electronics and Drives with Aalborg University, in 1992, 1996, and 1998, respectively. In 2017, he became a Villum Investigator. He is honoris causa with University Politehnica Timisoara (UPT), Romania, and Tallinn Technical University, Estonia. He has published more than 600 journal papers in the fields of power electronics and its applications. He has coauthored four monographs and an Editor of ten books in power electronics and its applications. His current research interests include power electronics and its applications, such as in wind turbines, PV systems, reliability, harmonics, and adjustable speed drives.

Dr. Blaabjerg has received 33 IEEE Prize Paper Awards, the IEEE PELS Distinguished Service Award in 2009, the EPE-PEMC Council Award in 2010, the IEEE William E. Newell Power Electronics Award 2014, the Villum Kann Rasmussen Research Award 2014, the Global Energy Prize in 2019, and the 2020 IEEE Edison Medal. He was the Editor-in-Chief of the IEEE TRANSACTIONS ON POWER ELECTRONICS from 2006 to 2012. He has been a Distinguished Lecturer for the IEEE Power Electronics Society from 2005 to 2007 and for the IEEE Industry Applications Society from 2010 to 2011 as well as 2017 to 2018. From 2019 to 2020, he served as a President of IEEE Power Electronics Society. He has been a Vice-President of the Danish Academy of Technical Sciences. From 2014 to 2020, he is nominated by Thomson Reuters to be between the most 250 cited researchers in Engineering in the world.